Synthesis of gold-silica core-shell nanoparticles by pulsed laser ablation in liquid and their physico-chemical properties towards cancer photothermal therapy

Authors

René Riedel[1], Nora Mahr[1], Chenyang Yao[2], Aiguo Wu[2], Fang Yang[1,2*], Norbert Hampp[1*]

[1]Physical Chemistry department of University of Marburg, Marburg, Germany

[2]Cixi Institute of Biomedical Engineering, CAS Key Laboratory of Magnetic Materials and Devices & Key Laboratory of Additive Manufacturing Materials of Zhejiang Province, Ningbo Institute of Materials Technology and Engineering, Chinese Academy of Sciences, Ningbo 315201, P.R. China

[*] Corresponding authors: hampp@uni-marburg.de; yangf@nimte.ac.cn

Supplementary Information

I) Experimental Setup

The experimental setup is shown in figure S1. Briefly, a ns-pulsed Nd:YAG laser was focussed onto a gold target by means of an optical lens with 100 mm focal length. The gold target was immersed in an

aqueous solution containing sodium chloride and different concentrations of sodium silicate. The target was rotated and struck by the laser pulses, which resulted in nanoparticles (NP) production.

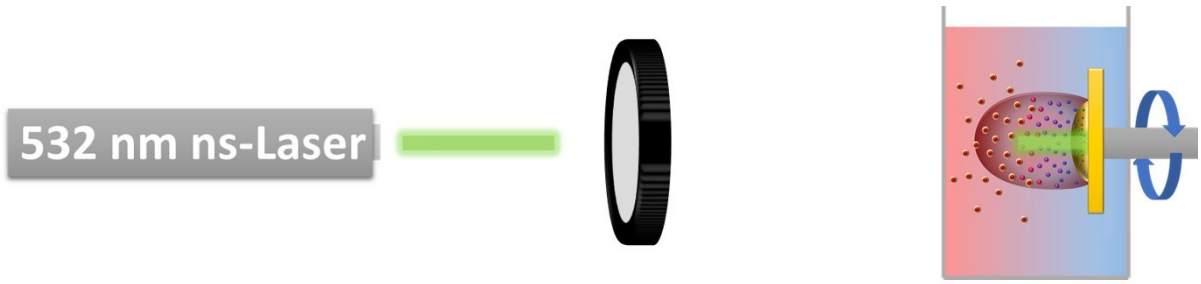

Figure S1 - Experimental setup. A 532 nm ns-laser shots laser pulses towards a target. These laser pulses are focussed using an optical lens with 100 mm focal length. The target is placed within a vessel containing bidestilled water, sodium silicate and sodium chloride. The target is rotated in order to increase the nanoparticle yield. The distance between optical lens and target is adapted in order to set the pulse focus directly behind the target.

II) Size distribution, DLS and Zeta Measurements

First tests showed that NP core and coating size varied with laser settings and soluble glass concentration as can be seen in figure S2. It is remarkable that the coating thickness did not depend on soluble glass concentration but rather on laser settings. Note that these data were obtained with a significantly smaller number of NP than for the final evaluation of NP size distribution which is shown in figure S3 C).

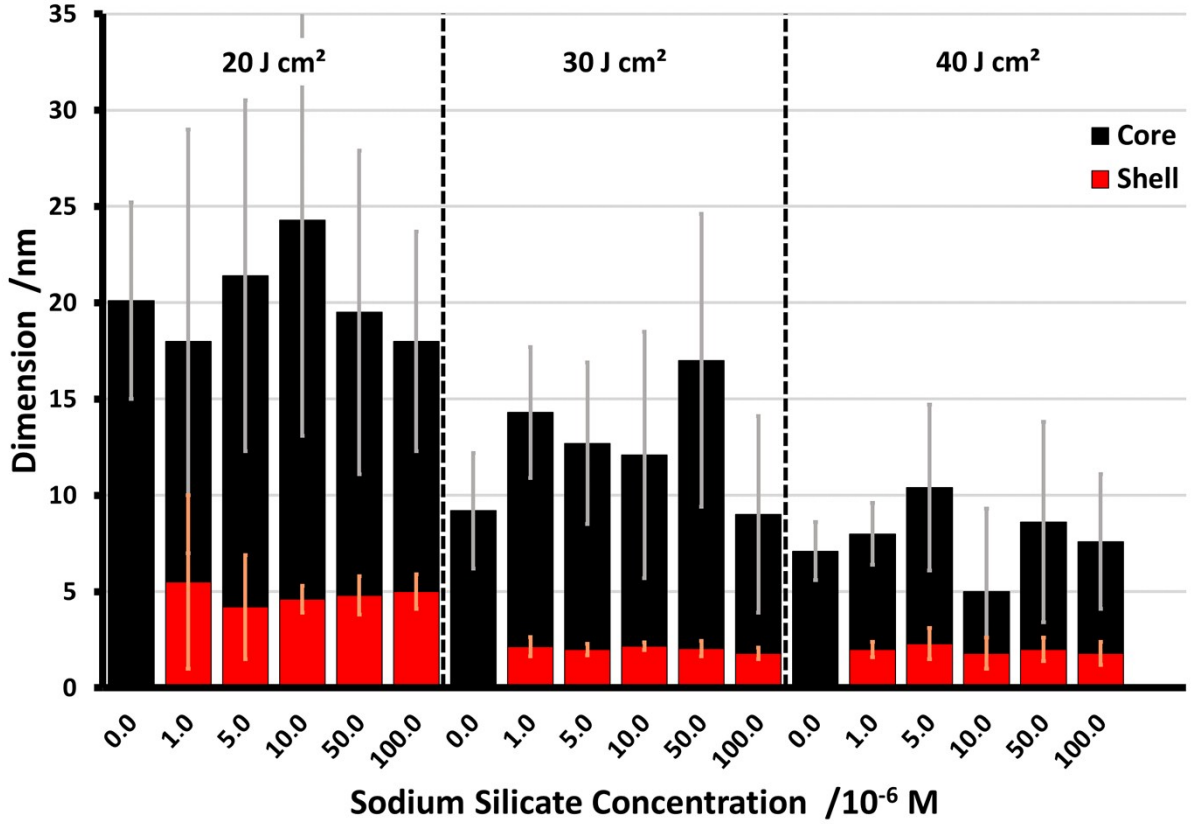

Figure S2 – Overview of core diameter and shell thickness for Au@SiO2 NP after synthesis with different laser pulses and sodium silicate concentration. As can be seen, shell thickness hardly varies with sodium silicate concentration (cf. small error bars). By trend, core diameter decreases with pulse power.

Since we encountered some problems concerning the stability of the glass vessel at $40\,J \cdot cm^2$, we chose to continue with $30\,J \cdot cm^2$ and $1 \cdot 10^4$ M sodium silicate concentration.

The evaluation of 3386 SEM pictures revealed a narrow size distribution shown in figure S3. The mean core diameter was 9 nm while the coating had a thickness of 2 nm.

The hydrodynamic diameter of the molecules was determined by means of dynamic light scattering[1] (DLS). DLS is an analytical method to investigate the hydrodynamic size of particles in a solution by means of the detection of scattering light from a laser beam going through that sample. The hydrodynamic diameter of the NPs describes the diameter of a NP including the solvation molecules that are tightly bound to the NP surface. These solvation molecules increase the effective diameter of

the NP and influence its diffusional and adhesive behaviour. It is hence important to determine the hydrodynamic diameter for behaviour interpretation. Figure S3 shows the measurement results of the hydrodynamic size.

ζ-Potential was measured using the Doppler effect in combination with electrophoretic mobility of the NP. It describes the electric potential at the shearing layer of a moving NP in solution and thus the surface charge of the hydrodynamic NP sphere. Hence, a high absolute value of ζ-potential results in repulsion of NP and leads to high stability. The results of ζ-potential measurements over 208 samples is shown in figure S5. The mean ζ-potential of -58.7 mV is in accordance with the long stability observed by means of UV/VIS spectra.

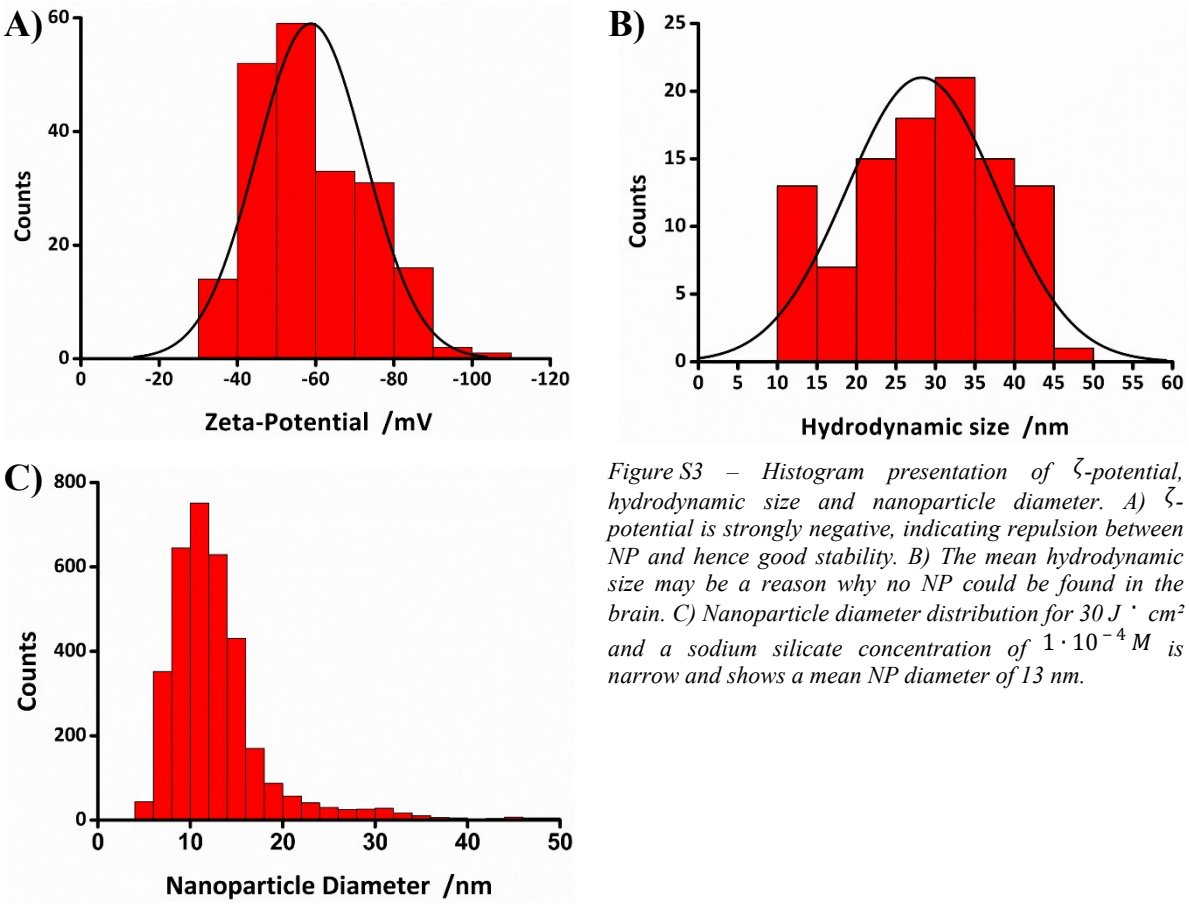

Figure S3 – Histogram presentation of ζ-potential, hydrodynamic size and nanoparticle diameter. A) ζ-potential is strongly negative, indicating repulsion between NP and hence good stability. B) The mean hydrodynamic size may be a reason why no NP could be found in the brain. C) Nanoparticle diameter distribution for 30 J · cm² and a sodium silicate concentration of $1 \cdot 10^{-4} M$ is narrow and shows a mean NP diameter of 13 nm.

III) PLAL Formation Mechanism

According to previous studies of PLAL[2–4], the production route of our synthesized Au@SiO_2 NPs can be derived, although the formation mechanism is not yet fully understood. As a laser pulse strikes the gold target, a plasma is built on the target surface, reaching temperatures up to 105 K and pressures up to several GPa. This plasma includes highly energetic clusters and ions that were ejected from the

target, in our case gold ions and clusters. Plasma expansion is accompanied by the formation of a shock wave. The confined plasma transfers its energy to the surrounding liquid, thereby vaporising the liquid and building a cavitation bubble. Energy transfer happens very fast and leads to cooling down and shrinking of the plasma. Recombination of the plasma species results in the formation of NP seeds, i.e. gold seeds in our experiment. After the extinction of the plasma, the gold seeds are ejected into the cavitation bubble, which itself consists of species derived from the surrounding liquids, particularly radicals and ions. In our case, it was mainly radicals and ions from water and silicon, such as OH-, OH·, O-, Si· and so on. Inside the cavitation bubble, the gold seeds grow to NPs. Normally, their size and size distribution depend on the lifetime of the bubble and hence on the laser pulse energy and liquid properties. In our case, however, the building of a silica shell confines the growth of the NPs, resulting in rather small NPs with a narrow size distribution. As the inner pressure of the cavitation bubble is equalised by the liquid pressure, the bubble reaches its maximum size and shrinks afterwards, releasing the silica gold NP into the surrounding liquid. While the plasma has a lifetime of about 3 µs, the cavitation bubble collapses after ~300 µs. Subsequent laser pulses are ablated by the NPs and lead to recrystallization and damping of the intensity of the incoming laser pulses. Hence, the solution must be renewed every 30 minutes.

IV) Force Spectroscopy

Recently, NP elasticity has emerged as an important parameter for cell incubation[5–7]. By means of force spectroscopy, mechanical properties of a NP can be extracted from force-distance curves. For this purpose, the right model must be chosen.

Force spectroscopy is applied using an atomic force microscope[8,9]. The main principle of measurement comprises the detection of interaction forces between the sample and a very sharp nanotip. The tip is located at the end of a cantilever, which itself is fixed to a bulk silicon board. As the tip approaches the sample, the cantilever is deflected from its initial position due to attractive or repulsive forces between tip and sample. The deflection can be measured using a laser that is focussed onto the backside of the cantilever. The reflected laser spot is trapped by a photodiode. As the cantilever is deflected, the spot position of the reflected laser beam on the photodiode changes. From this change, the interaction forces between tip and sample can be calculated if deflection sensitivity (i.e. ratio of deflection of the cantilever to spot position change on photodiode, nm/V) and the spring constant of the cantilever (N/nm) are known.

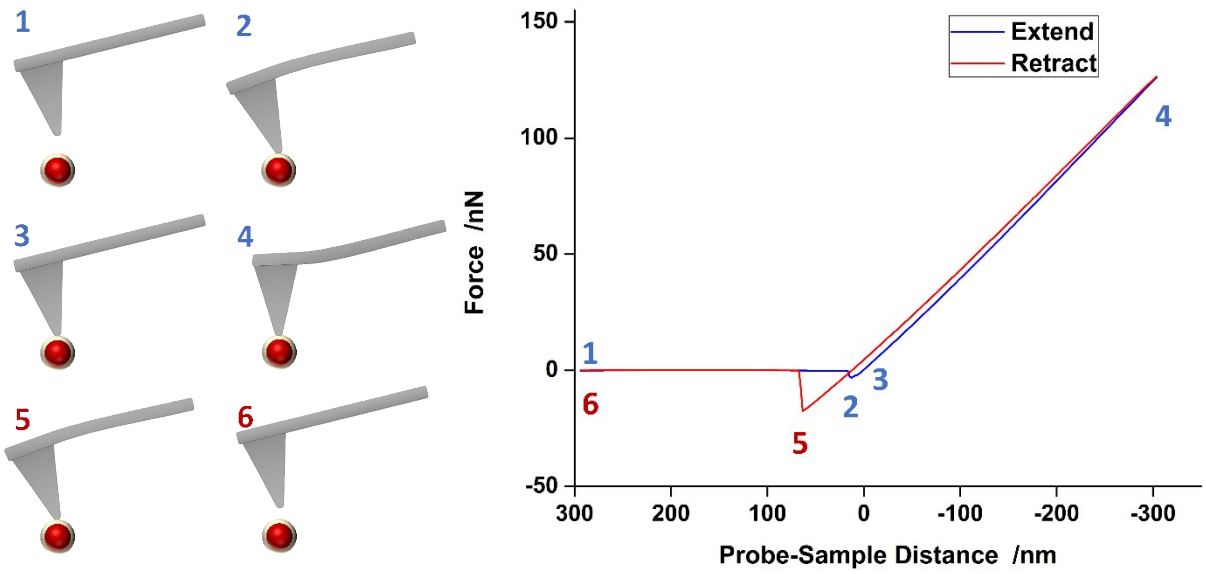

Figure S4 – Indentation process (left) and resulting force-distance curve (right). First, the tip is located above the sample to be measured (1). When the tip is approached to the sample (extended), attractive forces increase until they surpass the restoring force of the cantilever. The cantilever suddenly bends towards the sample (Snap-On, (2)). Here, the applied force is negative, indicating attraction between tip and sample. Further approaching leads to an increase of repulsive forces. At (3), repulsive and attractive forces cancel, and the force is zero. This point is referred to as contact point. As the indentation continues, the force between tip and sample increases about linearly. At a certain point, the approaching is stopped (4) and the tip is retracted. Due to adhesion forces, attractive forces are greater than for approaching. Just when the total amount of attractive forces become smaller than the restoring force of the cantilever, contact is lost (Snap-Off, (5)). After further retraction, the tip reaches its initial position at zero force (6). Adhesion forces can be read out from the force at (5) while elasticity can be calculated from the slope between (4) and (5).

At force spectroscopy, the tip is located above the sample to be examined. The tip is approached vertically to the sample and the interaction force between tip and sample is plotted versus the relative cantilever vertical position. At a certain point, the cantilever is retracted from the sample until it reaches its initial vertical position. Figure S4 shows a typical force-distance curve. At the initial position 1, the tip is not in contact with the sample and the interaction force between these both is negligible. As the tip is approached, attractive forces increase until they overcome the cantilever resistance to deflection. At this point, the cantilever is suddenly deflected towards the sample. This is called the Snap-On point and labelled as point 2 in Figure S4. As the approaching proceeds, repulsive forces become stronger and finally dominate. The force-distance plot is nearly linearly. After a certain indentation depth (4), the tip is retracted from the sample. The interaction forces decrease linearly with the cantilever position until attractive forces excel the repulsive forces (5). The attractive forces may be larger for retraction than for extending due to adhesion forces. When the restoring force of the cantilever excels the attractive force between tip and sample, the tip-sample contact abruptly breaks and the interaction force cancels to zero. This point is referred to as Snap-Off point (6).

From the slope at the region of repulsive interaction between tip and sample elasticity can be calculated. To do so, the native curve must be modified as follows. For each step, both retraction and extension are treated separately.

In the non-contact region of the force-distance curve, the force must be set to zero. To do so, a linear regression function is drawn from the data of the non-contact region. This function is subtracted from all data points of the force-distance curve.

For further calculations, the axis of abscissas must be adapted so as to choose the tip-sample contact point as the point of origin[10,11] and positive abscissa values toward the slope. The choice of an adequate contact point is as important as it is difficult. In this work, we ordained as contact point the point where the sum of repulsive and attractive forces in the contact region equals zero.

In this adapted system of coordinates, adhesion can easily be extracted from the lowest force value of the retracting curve. In order to calculate the elasticity of the NP, the extracted slope must be further modified. For elasticity calculation, the behaviour of the interaction force relative to indentation depth is important. However, the axis of abscissa does not provide the actual indentation depth of the tip but rather the position of the cantilever. Equation S1 can be used to calculate the indentation depth δ_i of the i-th data point from the cantilever position z_i, using the force values F_i and the spring constant k of the cantilever.

$$\delta_i = z_i - \frac{F_i}{k} \tag{S1}$$

V) Contact Mechanism Models

The behaviour of two bodies in contact depends on the applied force and on the properties of the bodies. In 1882, Hertz[12] mathematically described the contact mechanism a rigid sphere indenting into a rigid half-space. His calculations resulted in the general equation S2 with adaptable parameters λ and β, which is only valid if no adhesion effects arise.

$$F = \lambda \delta^{\beta} \tag{S2}$$

λ and β depend on the shape of the bodies in contact. For the Hertz model of a rigid sphere with radius R, indenting a rigid half-space, equation S2 becomes equation S3.

$$F = \left[\frac{4 \quad ER^{\frac{1}{2}}}{3(1-\upsilon^2)}\right]\delta^{\frac{3}{2}} \tag{S3}$$

υ is the Poison ratio of the sample. A tip with a tip radius R can be seen as a sphere if the indentation depth does not exceed R. Hence, from the slope of the interaction force F versus the indentation depth δ power 1.5, the elasticity modulus can be calculated when R and υ are known. This model is also valid for contact mechanism calculations of two rigid spheres. Further models were developed for different shapes of bodies in contact. For example, Sneddon[13] adapted the Hertz equation for a sharp cone intending a half-space. This model is commonly used in case the dented body is plane or has a radius much larger than the radius of the penetrating body, while the penetration depth is large. In this case, the penetrating body can be approximated as a cone.

Nevertheless, the Hertz-based contact mechanism models exhibit some restrictions. The two bodies in contact must be perfectly smooth and no other forces as friction or adhesion occur. Although these requirements rarely are met, the Hertz model leads to acceptable results in certain cases.

In case adhesion forces are present, the Hertz equation is inaccurate. In 1975, Derjaguin, Muller and Toporov[14] developed a theoretical model (DMT model) by evaluating the addition of adhesion force F_{adh} to the Hertz model. They assumed that adhesion only occurred within the contact region and is directed parallel to the indentation axis. Equation S4 shows the relation between F and δ.

$$F = \left[\frac{4}{3(1-\upsilon^2)} E R^{\frac{1}{2}}\right] \delta^{\frac{3}{2}} - F_{adh} \tag{S4}$$

Almost at the same time, Johnson, Roberts and Kendall[15] proposed a model considering a local deformation of the sample near the contact area due to adhesion forces at the retract process, therefore enhancing the contact area (JKR model). This description can be represented as in equation S5.

$$\delta = \frac{1}{R} \cdot \left[\frac{3}{4} \cdot \frac{E \cdot R}{(1-\upsilon^2)} \left(\left(F_{adh}\right)^{\frac{1}{2}} + \left(F + F_{adh}\right)^{\frac{1}{2}} \right)^2 \right]^{\frac{2}{3}} - \frac{4}{3} \left(\frac{3 \cdot E \cdot F_{adh}}{4(1-\upsilon^2) \cdot R} \right) \tag{S5}$$

These two different models are the constricting extrema of the real value range, where soft and flexible material tends to deformation and is better described by JKR. Rigid samples with low adhesion forces tend to have values close to DMT calculations.

Figure S5 shows a comparison of the Hertz, JKR and DMT models.

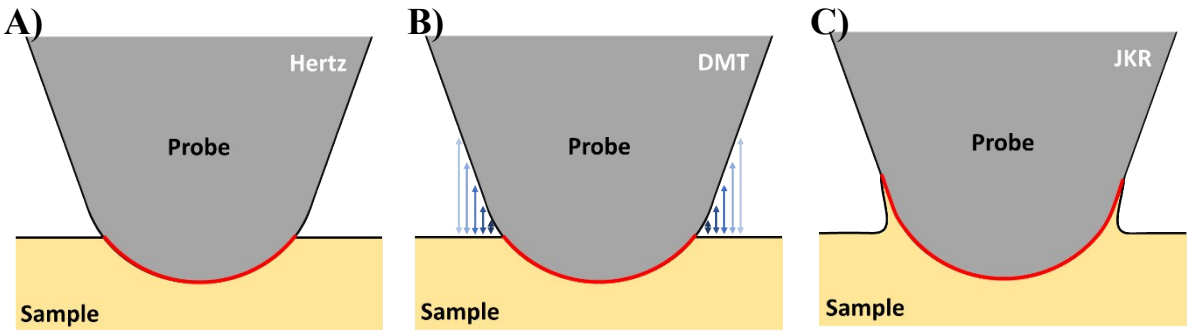

Figure S5 – Different Contact Mechanics Models. A) The Hertz-Model describes the contact mechanism of a rigid sphere intended whether into a rigid plane or into another rigid sphere. The area of contact (red) is determined by the radius of the intending sphere as well as the indentation depth. Adhesion forces are neglected. B) The DMT model considers adhesion forces outside and close to the contact area. The model is based on the Hertz model, the contact area remains the same as with Hertz. C) The JKR model considers adhesion forces which result in sample deformation near the intender. The contact area changes with adhesion.

In our work, the force distance curves clearly revealed adhesion forces, as can be seen from Figure S3. Accordingly, elasticity was calculated by means of the DMT and JKR model. For comparison, the Hertz model was also evaluated. Figure S6 shows the adhesion forces and elasticity values. The real value is expected to be closer to DMT, since the silica shell probably is not prone to deformation.

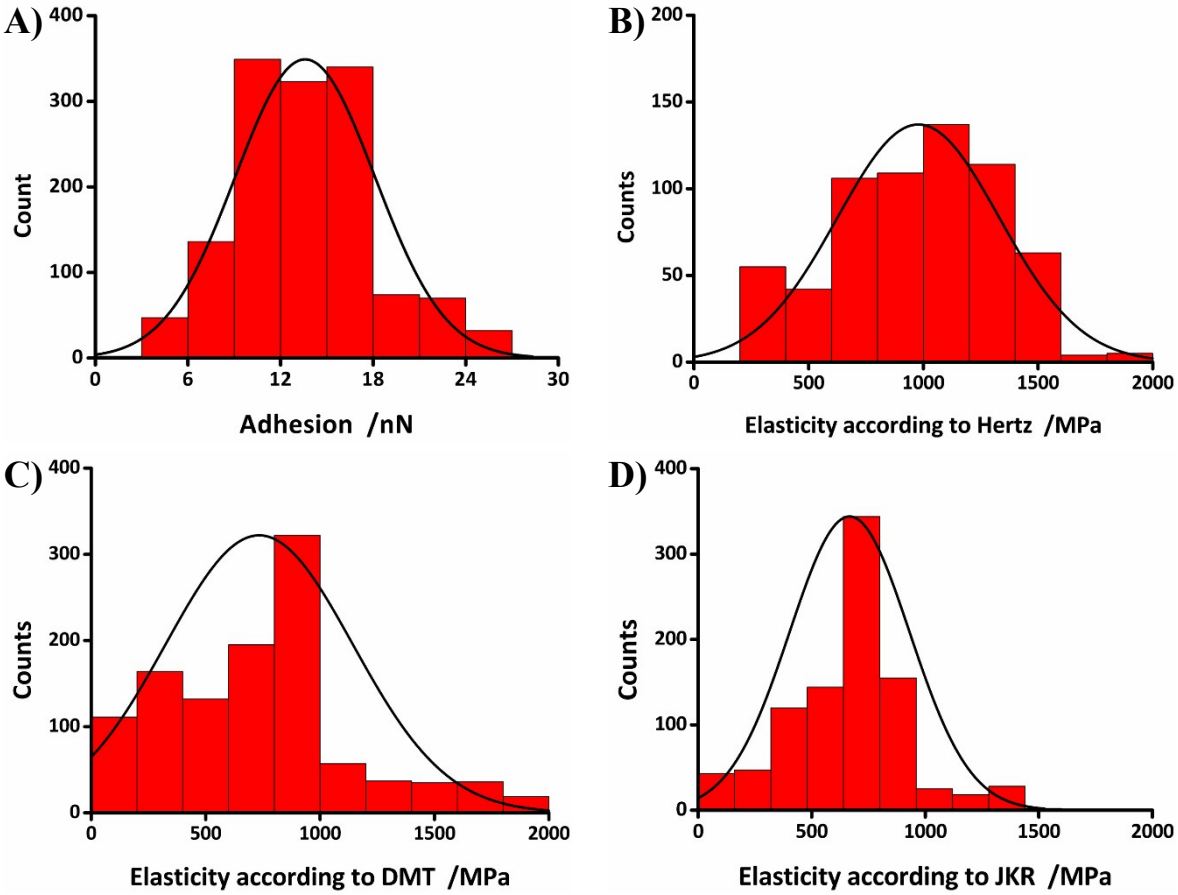

Figure S6 – Evaluation values for mechanical property measurements. A) Adhesion forces. B) Histogram representation of the elasticity according to the Hertz model. Not all the data could be evaluated with this model. C) Elasticity according to DMT model. D) Elasticity by JKR theoretic model. Comparison between Hertz, DMT and JKR show little difference between DMT and JKR, while Hertz distribution maximum is higher than with the two other models.

VI) BSA Coating

Bovine Serum Albumin (BSA, Merck, Germany, purity > 97 %) was used to proof the simplicity of ligand and protein binding. 10 µl BSA (6.45 · 10-7 mol/l) and 10 µl Au@SiO2 NP (1.77 · 10-8 mol/l) were mixed with a hydrochloric acid solution (pH 4.5). The solution was shaken for 30 minutes and centrifuged for 5 min at 5000 rpm afterwards. The supernatant was taken away and analysed by means of electron microscopy and atomic force microscopy. Figure S7 shows an electron microscopy picture. To ensure the BSA coating was successful, atomic force microscopy was used to measure topography and elasticity. At figure S7 B, the topography is shown. Positions with largely lower elasticity than the hard silicon wafer substrate are enlighten with greenish colour.

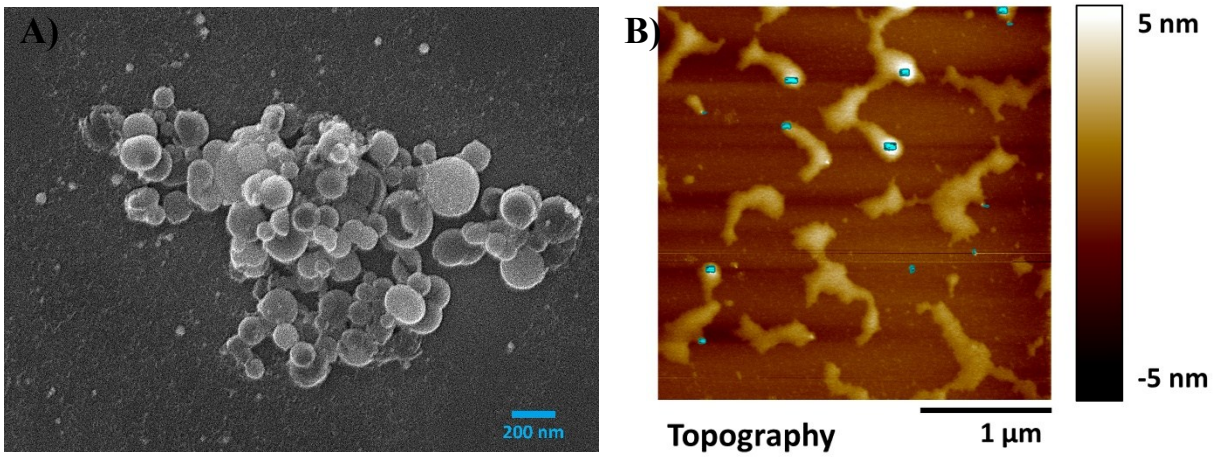

Figure S7 – BSA coated Au@SiO_2 nanoparticles. A) Scanning electron microscopy record of albumin coated Au@SiO_2 NP. The diameters of the particles were between 100 and 200 nm which was an indication but not a proof for BSA coating. B) Atomic Force Microscopy measurement of a sample. The greenish points indicate locations with elasticity that largely varied compared to the elasticity of the other positions. Elasticity was measured by means of PeakForce™ Tapping Mode[16].

VII) Real-Time Cell Viability Monitoring

Cell viability tests were performed using a method invented by Fang et al[17]. Cells were adsorbed onto an oscillating cantilever. Driving the oscillation at constant frequency, the amplitude of the oscillation depends on the overall mass of the oscillating system. By increasing the mass of the system, the amplitude rises, and vice versa. So, when a cell is adsorbed onto the cantilever, the mass of the oscillating system is increased, and the amplitude rises. Adding a toxic substance to the system leads to apoptosis of the cell and to a loss of its adsorption forces, resulting in detachment of the cell from the cantilever and a subsequent decrease in oscillation amplitude. Thus, the viability of cells can be observed by recording the amplitude of the oscillation and plotting it versus time.

Figure S6 shows the measurement of HeLa cells incubated with 12 nM Au@SiO2 NP. At first, cells are added to the system in nutrient solution. After 30 minutes, the system is equilibrated, and the amplitude has a constant value. Hereupon, NP solution is added. An increase in amplitude can be observed due to the presence of NP, reaching a maximum value. In case these NP have any toxic

effect to the cells, the amplitude begins to decrease. The amplitude decreases exponentially (except if there is no toxic effect) and can be expressed as in equation S6.

$$A_i = A_0 \cdot e^{-B \cdot t_i} \quad \text{(S6)}$$

Where A_0 is the maximum amplitude of the measurement, A_i is the amplitude at a given point i at time t_i, and B is the damping constant that describes the detachment rate of mass from the cantilever and hence is strongly related to apoptosis and the toxic effect of the added substance.

Figure S8 shows the measurements applying Au@SiO2 NP with different concentrations to HeLa cells. The corresponding B-values are listed in the table at the right side of figure S8. The values and measurements can be construed as proof for very low acute toxic effect of the synthesized Au@SiO2 NP.

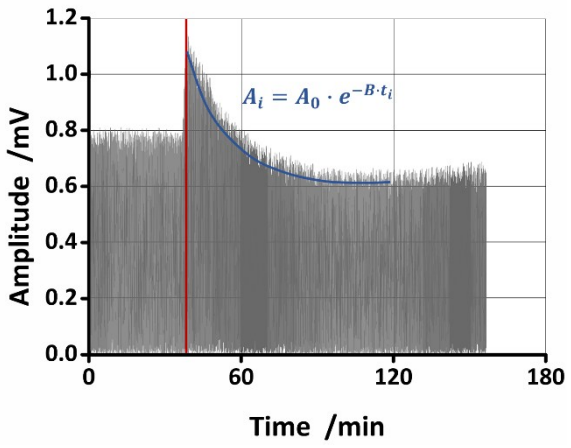

NP concentration	B-value
12 nM	$6.945 \cdot 10^{-5}$ s^{-1}
6 nM	$4.988 \cdot 10^{-5}$ s^{-1}
3 nM	$4.001 \cdot 10^{-5}$ s^{-1}
1.5 nM	$3.423 \cdot 10^{-5}$ s^{-1}

NP concentration	Cell viability
12 nM	87.83 %
6 nM	90.96 %
3 nM	93.26 %
1.5 nM	94.81 %

Figure S8 – Real-time cell viability data curve (left) and cell viability data (right). In order to evaluate the real-time cell viability measurement, the measured data are modified. The absolute values are taken, and outliers are ejected. The graph on the left shows the so-obtained data curve. NP were added after 36 minutes. After the amplitude reaches a maximum (red line), it decreases exponentially according to equation XF (blue line). The calculated B-values (upper right) result from slight amplitude decreases over time and hence indicate very low acute cell toxicity, which is in accordance with resazurin cell viability test values (lower right). In conclusion, the nanoparticles are not toxic to cells at given concentrations.

VIII) References

[1] W. I. Goldburg, *Am. J. Phys.* **1999**, *67*, 1152–1160.

[2] M. Dell'Aglio, R. Gaudiuso, O. De Pascale, A. De Giacomo, M. Dell'Aglio, R. Gaudiuso, O. De Pascale, A. De Giacomo, *Appl. Surf. Sci.* **2015**, *348*, 4–9.

[3] A. De Giacomo, M. Dell'Aglio, A. Santagata, R. Gaudiuso, O. Pascale, P. Wagener, G. Messina, G. Compagnini, S. Barcikowski, *Cavitation Dynamics of Laser Ablation of Bulk and Wire-Shaped Metals in Water during Nanoparticles Production*, **2013**.

[4] S. Reich, P. Schönfeld, P. Wagener, A. Letzel, S. Ibrahimkutty, B. Gökce, S. Barcikowski, A. Menzel, T. dos Santos Rolo, A. Plech, et al., *J. Colloid Interface Sci.* **2017**, *489*, 106–113.

[5] S. L. Tao, T. A. Desai, *J. Control. Release* **2005**, *109*, 127–138.

[6] K. A. Beningo, Y. Wang, *J. Cell Sci.* **2002**, *115*, 849 LP – 856.

[7] X. Yi, X. Shi, H. Gao, *Phys. Rev. Lett.* **2011**, *107*, 98101.

[8] G. Binnig, C. F. Quate, C. Gerber, *Phys. Rev. Lett.* **1986**, *56*, 930–933.

[9] B. Cappella, P. Baschieri, C. Frediani, P. Miccoli, C. Ascoli, *IEEE Eng. Med. Biol. Mag.* **1997**, *16*, 58–65.

[10] D. C. Lin, E. K. Dimitriadis, F. Horkay, *J. Biomech. Eng.* **2006**, *129*, 430–440.

[11] D. C. Lin, E. K. Dimitriadis, F. Horkay, *J. Biomech. Eng.* **2007**, *129*, 904–912.

[12] H. Hertz, *J. für die reine und Angew. Math. (Crelle's Journal)* **1882**, *1882*, 156.

[13] I. N. Sneddon, *Int. J. Eng. Sci.* **1965**, *3*, 47–57.

[14] B. V Derjaguin, V. M. Muller, Y. . Toporov, *J. Colloid Interface Sci.* **1975**, *53*, 314–326.

[15] K. L. Johnson, K. Kendall, A. D. Roberts, *Proc. R. Soc. London* **1971**, *324*, 301–313.

[16] B. Pittenger, in *Nanomechanical Anal. High Perform. Mater.* (Ed.: A. Tiwari), Springer Netherlands, **2014**, pp. 31–51.

[17] F. Yang, R. Riedel, P. del Pino, B. Pelaz, A. H. Said, M. Soliman, S. R. Pinnapireddy, N. Feliu, W. J. Parak, U. Bakowsky, et al., *J. Nanobiotechnology* **2017**, *15*, 23.